Real-Time Visualization of 3D Amyloid-Beta Fibrils from 2D Cryo-EM Density Maps

H. Kniesel[1] and T. Ropinski[1] and P. Hermosilla[1]
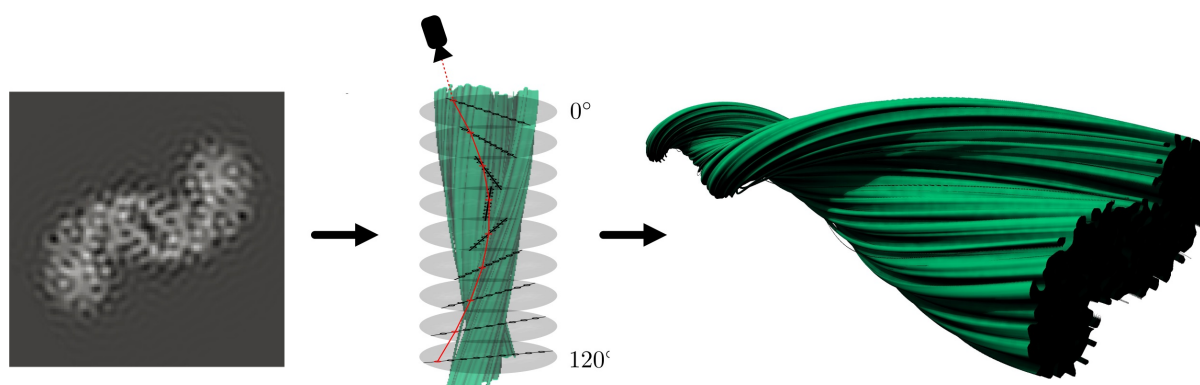
[1]Ulm University, Germany

Figure 1: *Pipeline of 3D model visualization of a fibril with helix structure from a 2D density map. The density map is extracted from the Electron Microscopy Data Bank (EMDB) with accession no. 3132*

Abstract

Amyloid-beta fibrils are the result of the accumulation of misfolded amyloid precursor proteins along an axis. These fibrils play a crucial role in the development of Alzheimer's disease, and yet its creation and structure are not fully understood. Visualization is often used to understand the structure of such fibrils. Unfortunately, existing algorithms require high memory consumption limiting their applications. In this paper, we introduce a ray marching algorithm that takes advantage of the inherent repetition in these atomic structures, requiring only a 2D density map to represent the fibril. During ray marching, the texture coordinates are transformed based on the position of the sample along the longitudinal axis, simulating the rotation of the fibrils. Our algorithm reduces memory consumption by a large margin and improves GPU cache hits, making it suitable for real-time visualizations. Moreover, we present several shading algorithms for this type of data, such as shadows or ambient occlusion, in order to improve perception. Lastly, we provide a simple yet effective algorithm to communicate the uncertainty introduced during reconstruction. During the evaluation process, we were able to show, that our approach not only outperforms the Standard Volume Rendering method by significantly lower memory consumption and high image quality for low resolution 2D density maps but also in performance.

CCS Concepts

• Human-centered computing → Scientific visualization; • Computing methodologies → Rendering; Computer graphics;

1. Introduction

Alzheimer's disease is a chronic disease and the cause of between 60 and 70 percent of dementia cases worldwide [Org19]. Despite its relevance, Alzheimer's disease is poorly understood. One of the main hypotheses of the causes of the disease is the formation of amyloid-beta fibrils in the brain [HA91]. These fibrils are

formed by the accumulation of misfolded amyloid precursor proteins along an axis. To gain insights on the structure of such fibrils, researchers have tried to reconstruct its atomic structure from cryo-EM imaging [CC17]. To visualize 3D models of amyloid-beta fibrils, reconstruction software is used to first create 3D density maps. The most generally applicable approach of 3D reconstruction is the

so-called single particle reconstruction (SPR) [ZSX*08]. This approach works best for well-ordered and rigid filaments [RG14], but when it comes to flexible and thin amyloid-beta fibrils SPR reaches its limits. Hence, specially designed 3D reconstruction software, like Relion [Sch20] and Frealix [RG14], can be used.

Rohou and Grigorieff [RG14] record, that prior knowledge of amyloid-beta fibrils suggests the conservation of axial order and the general assumption of amyloid-beta fibrils being featureless along the axial direction, specifically at resolutions greater than 4.8Å. Based on this assumption, they create a reconstruction which defines helix parameters at specified key points along the fibril's axis. Also, Relion [Sch20] uses prior information of the axial symmetry for helical reconstruction. It generates a model with the highest probability of describing the underlying micrographs. Due to the ability of Relion to estimate most reconstruction parameters without requiring user input, it is nowadays a commonly used software tool. The result of this reconstruction is a 2D map in which each pixel encodes the electron density at this particular region of a horizontal cut of the fibril (see Figure 1). But, although the resulting 2D density maps can provide an initial overview of the structure of the fibril's cross-section, these maps ignore a crucial parameter of the fibrils: the rotation angle along the main axis. This parameter is needed to explain the features of the underlying structure. To provide a complete overview of the fibril, 3D visualization is required. The most commonly used technique for such visualization is to create a 3D density map [NS15], and apply volume rendering to generate the final image [SC18]. This technique allows to apply different transfer functions to interactively inspect the 3D reconstruction. However, such a technique requires high amounts of GPU memory and expensive rendering algorithms to generate the final image. Especially, in the case of visualizing long sections of a fibril, volume data becomes large, so that this data is usually visualized piece by piece, showing smaller sections of the fibril. A complete visualization of the fibril is hence neglected. Further, based on the needed trilinear interpolation during volume rendering, artefacts can be introduced, especially for low resolution data. Those artefacts can then lead to a misinterpretation of the underlying data.

Moreover, the process of 3D reconstruction is not able to exclude noise, which is introduced during the collection and generation of the underlying micrographs [MOA18]. Particularly, due to the flexible nature of amyloid-beta fibrils, small variations of atom positions between the different cross-sections of the fibril, depicted in micrographs, introduce uncertainty in the model structure. Further, beam-induced movements, ice contamination, noise introduced by the electron microscope [RG14], or the low resolution of the cryo-EM images, lead to uncertainty of the reconstructed model. This uncertainty is depicted in smooth gradients in the resulting density map: Low uncertainty is based on high atom occurrence (hence a high density) in the depicted area, encoded in white areas of the density map. On the other hand, little atom occurrence results in high model uncertainty, which is encoded as dark regions in the density map. This information has to be taken into account when analyzing the fibrils and, therefore, has to be effectively communicated by the visualization algorithm used. Nevertheless, the visualization of data uncertainty is usually neglected by the 3D visualization algorithms, even though awareness of model uncertainty is a crucial prerequisite for further decision making and processing of the visualization regarding molecular mapping and interpretation

of the data.

In general, it can be stated, that amyloid-beta fibrils are special in their structure. They usually create long filaments with an underlying coil. Hence, researchers require specialized tools for reconstruction as well as for visualization. Relion solves the request for specialized reconstruction tools. Still, there are no sufficient visualization tools, which make the visualization of large fibril sections possible.

Therefore, in this paper, we introduce a new real-time visualization algorithm to inspect 3D reconstructions of amyloid-beta fibrils, which, in contrast to previous techniques, only requires a small amount of GPU memory to store the fibril data. Thereby, we provide the possibility to visualize large sections of a fibril. Further, it can generate high-quality renderings based on low resolution 2D density maps. Our algorithm takes advantage of the inherent repetitions within the fibrils structures by modifying a ray marching algorithm to access the appropriate pixels in a rotated 2D density map. Lastly, we propose to visualize a semi transparent coat with the 3D fibril to provide a better understanding of the uncertainty of the model.

2. Related Work

3D reconstruction Based on the development of direct electron detector cameras as well as progress in image processing, near-atomic resolution can be reached by the molecular 3D reconstruction based on cryo-EM [Fra17]. In general, 3D reconstruction can be stated as the process to form a 3D image from random projection views retrieved from multiple micrographs.

As stated in Section 1, 3D reconstruction of amyloid-beta fibrils require specialized software to compensate for the special nature, as well as to integrate prior knowledge, to improve reconstruction results. This is due to the long and thin shape of the fibril. Software tools like Relion [Sch20] and Frealix [RG14] use prior information on symmetry along the fibril's axis to retrieve a more accurate reconstruction. Relion uses the prior information of the fibrils to project the micrographs and compute iteratively the most likely model which can be described by the underlying micrographs. Frealix, on the other side, uses the prior information to directly compute parameters of a coil structure (like pitch and repeat) at given key points along the fibril's axis.

Lastly, based on the 2D density maps the retrieved data can be visualized. This can be done to gain a more general and detailed overview of the underlying data. For example by using UCSF Chimera [PGH*04] surface rendering can be used. Moreover, molecular mapping based on the reconstruction can be applied to draw further conclusions. This gained knowledge can then be used to retrieve structural, hence functional, information of the processed structure. The gained information always relies on a complete communication of information encoded by the underlying data.

Hardware accelerated Volume Rendering Volume rendering is usually applied for the visualization of medical data like computer tomography (CT) and magnet resonance (MR) [EHK*04; DCH88; Pfi05; SB07]. Ray casting allows the separate calculation of each casted ray, making full use of the parallel computations on a GPU [EHK*04]. Different sources [RGW*03; EHK*04; Pfi05;

SB07] introduce specific hardware acceleration techniques, like early ray termination and (geometry-based) space leaping, which allow an efficient implementation of ray casting. Moreover, the adaption of resampling intervals during periods of user interaction and static visualizations can be used [SB07]. Resampling intervals can also be adapted regarding the level of detail shown, as well as the information density in the underlying data set [EHK*04].

Nowadays, volume rendering is scalable to generate interactive frame rates. For example, in 2019, J. Martschinke et al. [MHK*19] were able to introduce an adaptive temporal sampling approach for Monte Carlo path tracing, implementing global illumination techniques. This approach is based on an adaption of temporal aliasing of surface rendering. Their introduced approach was able to achieve interactive frame rates for Monte Carlo path tracing on volumetric data. Still, GPU computation power is primarily limited to memory and up/download bandwidth instead of computation power [Pfi05], resulting in a limitation of data set sizes, even though storing the underlying data in a texture exploits the high internal bandwidth of the GPU [EHK*04]. Investigation of medical data like CT or MRI usually consumes large memory space [RGW*03; EHK*04; PB07], pushing the limits of GPU memory space while accessing textures without spatial coherence [RGW*03]. The same applies for the visualization of large fibril filaments. Especially, because high-quality renderings require high-resolution 3D data. Hence, the use of sparse volume data is a common approach. In sparse volume data only occupied voxels are saved in memory, instead of saving a dense voxel grid. The percentage of saved memory depends on the underlying data. On the other side, sparse volume data requires additional data structures, to be accessed suitably during rendering. Hence, data access is usually slower as data access to standard dense grids. Optimizations of sparse data access and rendering are developed by multiple researchers, further enhancing the performance of the approach (for example [ZML19; ZSL19; LBG*15]).

Data uncertainty Even though, the technique of cryo-EM experienced major progress [Fra17], being able to reconstruct near-atomic resolution of imaged structures, limits of the technique are well known. Based on different noise sources in the imaging process, resulting micrographs are connected to high SNR. Noise disturbs the imaging process especially in the case of flexible and thin fibrils. Further improvement of visualization quality can be achieved by taking sample uncertainty, of the underlying cryo-EM data and the 3D reconstruction process, into account. Considering the uncertainty of the data is necessary to communicate all given information by the underlying data.

While there are approaches in Volume Rendering to visualize noisy data, without great influences of noise [SE16], it is crucial to also communicate the original presence of noise in the underlying data, since this kind of denoising in 3D visualizations can not be assumed to be error-free. In fact, visualization of uncertainty has developed as a research field in many elementary applications like biological science, geoscience, or medical imaging [DLD*15; Pan*01; SZD*10], where decision making based on the provided data (like planning a surgery) needs to be precise and well-considered.

In our approach, of visualizing 3D reconstructions of amyloid-beta fibrils, retrieved from cryo-EM images, deviation of structural and functional information, as well as mapping of molecules relies on the complete and correct visualization of the 3D reconstruction.

Different studies have shown, that the awareness of uncertainty in data, concludes to different decisions [Dei07; SMV*14]. This might be based on the fact, that visualizations, that model uncertainty can provide a more complete representation of the underlying data [PWL*97]. Researchers investigated different methods and application contexts to represent uncertainty. Approaches include side-by-side comparison [BHJ*14], modifying attributes like color or shading variables, adding glyphs [PWL*97; BHJ*14] or geometry [PWL*97], data overlay [BHJ*14] and many more. As Pang et al. [PWL*97] already investigated, approaches are suited differently well depending on the underlying data representation.

3. Ray Marching

In this section, we present a ray marching algorithm which reduces GPU memory use, making it possible to visualize large fibril filaments. Our algorithm uses a single 2D density map to generate an interactive 3D visualization of the amyloid-beta fibril. Prior structural information about the fibril is used to generate a 3D model: a 2D cross-section of the helix structure and the helix rotation. Our approach uses this prior information to transform texture coordinates according to the helix structure of the fibril. To take advantage of this prior information, instead of marching linear rays in space, we march non-linear rays. A schematic depiction can be seen in Figure 2. In other words, while marching a ray, we transform the mapped texture coordinates of each sample, based on the position of the sample along the longitudinal axis and the known rotation of the fibril. This has the same effect as rotating the texture based on an angle retrieved by the position of the sample along the fibril's axis and its total twist value, but without requiring additional memory. The twist of texture coordinates allows a differentiated evaluation of the underlying 2D density map at according positions. In the following, we will further refer to our approach as the non-linear ray marching.
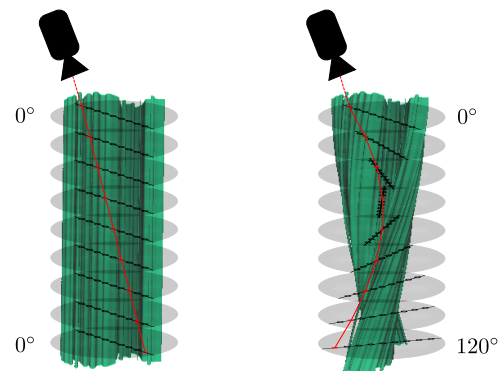

Figure 2: *Schematic model of the original ray marching (left) and the non-linear ray marching (right). In our approach, we rotate texture coordinates while marching linear rays in world space. This can be compared to twisting rays in world space.*

3.1. Standard Ray Marching

In standard ray marching, for each pixel, a ray is traced from the viewpoint through the pixel into the volume. Each ray is defined by

its direction ω and its step size η. Hence, each sample position p_i along a ray can be calculated through:

$$p_i = p_o + i \cdot \eta \cdot \omega \tag{1}$$

Usually, a bounding geometry is rendered, to skip empty space between the view plane and the surface. Hence p_0 determines the intersection of the ray and the bounding geometry. By using the positions p_i, a ray can be integrated in a discrete manner. Therefore, a suitable, finite number of maximum iterations, defining the maximum number of samples evaluated along a ray, needs to be defined. This number of maximum iterations can be optimized by terminating the ray if the integral reaches an opacity value of one.

3.2. Non-linear Ray Marching

Building on the standard ray marching, we implement an adapted version. As a bounding geometry, we use a cylinder, which can include a model of a fibril most tightly. To improve performance, we make the step size η adaptive, in such a way, that it is responding to visible details in relation to the zoom value d and the fibril's twist value t_f. Therefore, $\eta : R \to R$, with:

$$\eta(d, t_f) = \eta_0 - k_1 \cdot d - k_2 \cdot |t_f| \tag{2}$$

This is a simple linear function, which does not need much computation time itself. The current visible details d are $\in [0, 1]$. Further, the twist of the fibril visualization is taken into account, i.e. the rotation in degree of the fibril along its axis. Taking the twist into account is useful since high twist values (multiple repetitions in the coil) result in higher frequencies, so overstepping of important information might occur, if η is chosen to be too large. Simultaneously, while decreasing the step size, maximum iterations need to be increased. Based on the anti-proportional correlation of step size and maximum iterations, similar parameters as in Equation 2 are taken into account:

$$i_{max}(d, t_f) = i_0 + k_3 \cdot d + k_4 \cdot |t_f| \tag{3}$$

In this equation we refer to maximum iterations as i_{max}, which are dependent on an initial iteration definition i_0. Since the scale of η and i_{max} differ, those scales need to be taken into account by using different scaling values k_1, k_2, k_3, k_4. In our implementation we set $k_1 = 0.001$, $k_2 = 0.00002$, $k_3 = 50$, $k_4 = 0.2$, with initial values $\eta_0 = 0.009$ and $i_0 = 655$.

Moreover, to be able to keep η high, to decrease computation time, while still generating high-quality renderings without artefacts, we add a binary search to determine a more exact surface-ray intersection. With the additional binary search, we are not only able to generate a ray marching algorithm with high performance, but we are also able to suppress visible surface artefacts, since the binary search can return a more specific surface-ray intersection than it is possible by using the linear step sizes only.

Texture Mapping In the following, we will describe the texture mapping as mapping world space coordinates to texture coordinates, in such way, that the mapped texture coordinates lie on a stack of circles inside the bounding cylinder. Those circles are only used as a depiction of the formulas and are no circle meshes. We do that to be able to evaluate samples for discrete integration over a view ray. As stated above, the 2D density map needs to show

a horizontal cross-section of the fibril to be visualized. Then, this cross-section is mapped onto all circles, which are aligned along the fibril's axis, the same way. In the following, we are assuming, that the cylinder's axis as well as the fibril's axis are aligned with the z-axis in world space. Then, the texture mapping can be applied to each circle in such a way:

$$f(p_{xy}) = [(p_{xy} - \vec{v}_{xy}) + c_t] \cdot \frac{|c_t|}{r} \tag{4}$$

Here, p_{xy} denotes xy-coordinates of any sample point p_i in world space, along any marched ray, which should be mapped to texture space. $\vec{v}_{xy}$ represents the xy-coordinates of the cylinder center in world space. The textures center $= (0.5, 0.5)$ is given by c_t. And r describes the cylinder's radius, so that $|c_t|/r$ normalizes the mapped coordinate to texture space. Since the underlying density map depicts smooth grayscale gradients, a threshold $t_1 \in (0, 1]$ is fixed. This is done to unambiguously evaluate the texture at defined sample positions, retrieved from the ray marching. If the evaluated samples return a larger value than t_1, the sample is assumed to be inside the fibril. This value can be chosen interactively by the user. It defines the minimum density to be displayed as solid fibril and is directly correlated to the uncertainty.

Non-linear rays The core of our approach is the introduction of non-linear rays. We are able to achieve this by transforming texture coordinates based on an interpolated twist value along the fibril's longitudinal axis. Therefore, the twist of the fibril needs to be known. In the following, we will define this twist in degrees per total length of the fibril. For each sample, a relative twist value needs to be defined in relation to this total twist value of the fibril and the sample position along the fibril's axis. Then, each texture coordinate, calculated by $f(p_{xy})$ (Equation 4), needs to be transformed in relation to this relative twist value. To determine the position of the sample along the fibril's axis, we project the sample in world space onto this axis and normalize the result to $\in [0; 1]$, by $g : R^3 \to R$.

$$g(p_i) = \frac{\langle \vec{v}_{xyz}, p_i \rangle}{|\vec{v}_{xyz}|^2} \tag{5}$$

Here, $\vec{v}_{xyz}$ corresponds to the fibril's axis, which is in our case $Z = (0, 0, 1)^T$. p_i denotes the sample in world space which will be transformed to texture space in the following. $\langle \cdot, \cdot \rangle$ is used as dot product notation. We then calculate the rotation parameter by interpolating the total twist value of the fibril, using longitudinal level of p_i which is $g(p_i)$:

$$t(p_i) = g(p_i) \cdot twist \tag{6}$$

Next, we use this relative rotation parameter $t(p_i)$ to rotate the corresponding texture coordinates $f(p_i)$, computed by Equation 4, around the fibril's axis. Evaluating the computed texture coordinates then results in a twisted visualization of a fibril, defined by its absolute twist value, and the minimum density threshold t_1.

4. Illumination techniques

It is a common understanding, that advanced illumination techniques can enhance the depth and size perception of volumetric data. Based on findings and guidelines provided by [LR11] for desktop applications, which was later extended to related guidelines in virtual reality by [DRN*17], we choose to implement
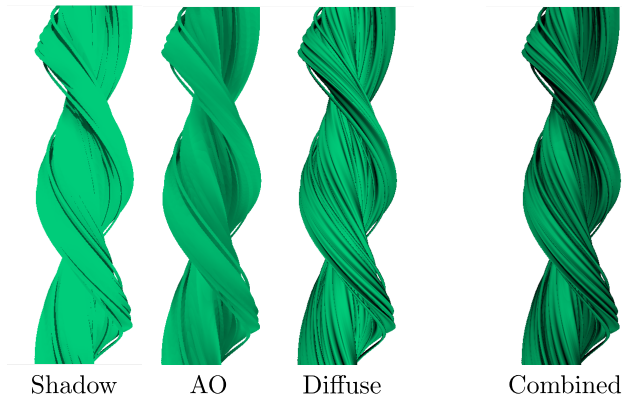
Shadow   AO   Diffuse   Combined

Figure 3: *Depiction of influence of the applied illumination techniques. As underlying density map, one 2D density map of the publication [SRL*15] is used. The high twist value is chosen independently of the reported structure, to stress effects of illumination.*

Figure 4: *Depiction of two sample points p_{t_1} and p_{t_2}, which determine the intersection of the view ray and the fibril's surface and coat, defined by minimum density thresholds t_1 and t_2, with $t_1 > t_2$. Those thresholds are used to define the semi transparent coat to communicate model uncertainty of the underlying 3D reconstruction. As underlying density map, one 2D density map of the publication [SRL*15] is used.*

different advanced illumination techniques for ray marching approaches. We simulate illumination in our scenes by splitting it into two main components: local illumination and global illumination. Local illumination is simulated using Phong shading [Pho75] whilst global illumination is simulated using an hybrid ambient occlusion algorithm [RBA09]. For the implementation of Phong illumination, surface normals are approximated using the central differences algorithm. Lastly, we further enhance the visualization by incorporating shadows. Effects of the applied illumination techniques can be seen in Figure 3.

Shadows are deployed through ray sampling in direction of the light source. For each surface point, a ray of fixed length l is marched in direction of the light source. To be able to observe the twisted surface of the fibril, in our case, we need to twist texture coordinates according to the description in 3.2, while marching rays.

Hybrid ambient occlusion was implemented similar to Reinbothe et al. [RBA09]. First, for each pixel, we approximate the ambient occlusion integral using Monte Carlo integration on a low number of rays. Different from Reinbothe et al. [RBA09] Hybrid ambient occlusion, we need to twist all texture coordinates while marching rays of the Monte Carlo integration in world space similar to the introduced non-linear ray marching in Section 3.2. Then, in order to reduce noise, we apply a bilateral filter that blurs the AO values, while preserving the edges at the same time.

5. Modeling of uncertainty

Lastly, uncertainty is modeled by the overlay of a semi transparent coat. As stated in Section 1, micrographs of cryo-EM have high SNR values. Specially, in the case of amyloid beta fibrils, the flexible and thin nature of the fibril leads to high sensitivity against the electron beam and small variations of atom positions between the different cross-sections of the fibril. Whilst rigid parts of the molecular structure can be reconstructed with relatively high fidelity, with areas of high density values in the 2D map, flexible parts are translated to large regions in the 2D map with relatively

low density values. Visualizing this information with a single fibril surface can lead to misinterpretations. Therefore, we define two isosurfaces defined by two thresholds t_1 and t_2. Similar to t_1, t_2 is a user defined value, which hence can be changed interactively. This second threshold defines the outline of a semi transparent coat, which we then render around the solid fibril. An illustration of that algorithm, can be seen in Figure 4. Therefore, it is required, that $t_1 > t_2$. This condition can be guaranteed, by defining t_2 in relation of t_1. The transparency of the coat is obtained by interpolating the color of the two isosurfaces defined by t_1 and t_2. The interpolation value is computed based on the distance between the two intersection points along the view ray, p_{t_1} and p_{t_2}. p_{t_1} is the intersection of the view ray with the isosurface defined by t_1, whilst p_{t_2} is the intersection of the ray with the isosurface defined by t_2. This distance $|p_{t_1} - p_{t_2}|$ is then further scaled by a sigmoidal function, to yield more realistic results.

$$i(|p_{t_1} - p_{t_2}|) = \frac{1}{1 + exp(-k \cdot |p_{t_1} - p_{t_2}|)} \quad (7)$$

In this equation k describes a scaling factor which can be set to adapt the value range of the function. In our case $k = 20$. Lastly, a user defined transparency term is added to make the transparency interactively changeable by the user. This user defined transparency t_{user} is included in the interpolation function of Equation 7 in the following way:

$$i(|p_{t_1} - p_{t_2}|, t_{user}) = (1 - t_{user}) \cdot i(|p_{t_1} - p_{t_2}|) + t_{user} \quad (8)$$

Lastly, $i(|p_{t_1} - p_{t_2}|, t_{user})$ is used to interpolate color and illumination values of the samples p_{t_1} and p_{t_2}. Since the calculation of Hybrid AO is rather costly, it is only applied to the solid fibril.

6. Implementation

In this section, we provide an overview of the three main steps (see Figure 5) of our implementation. **Step 1** In the first step we implement our non-linear ray marching, as it is described in Section 3.2. Further, for every surface point of the solid fibril, we calculate the presented illumination techniques in world space (see Section 4). We interpolate illumination values, except for the AO value, of the semi transparent coat and the solid fibril, as reported in Section 5. We save the used interpolation value as transparency term, which we will use in step three to interpolate color values, as well as the
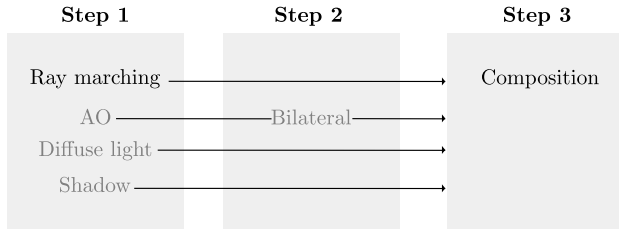
Figure 5: *Schematic representation of the three main steps of the approach. Since illumination calculation is no contribution of our paper, we marked them in light grey.*

Ours		Volume rendering		
dim.	mem.	dim.	mem.	sparse mem.
64^2	4 KB	$64^2 \times 256$	1048 KB	182 KB
64^2	4 KB	$64^2 \times 2048$	8 MB	1452 KB
128^2	16 KB	$128^2 \times 512$	8 MB	1461 KB
128^2	16 KB	$128^2 \times 4096$	67 MB	12 MB
256^2	65 KB	$256^2 \times 1024$	67 MB	12 MB
256^2	65 KB	$256^2 \times 8192$	537 MB	93 MB
512^2	262 KB	$512^2 \times 2048$	537 MB	93 MB
512^2	262 KB	$512^2 \times 16384$	4 GB	746 MB

Table 1: *Memory comparison for different settings. All values are rounded. The default format for GPU memory is assumed (each voxel is stored in a byte). While the memory need of the non-linear ray marching does not increase with the length of the fibril, the memory regarding standard volume rendering increases significantly. Sparse mem. shows the memory occupancy for sparse volume data, saving only occupied voxels. Based on the EMD-3132 volume with a minimum density threshold of* 0.4*, a voxel occupancy of* 17% *is assumed.*

AO similarly. Further, we combine diffuse light and the computed shadow value by multiplication, to later save memory by forwarding the values to the next step. Regarding AO, we sample 6 rays inside a hemisphere of radius 0.2. Lastly, we compute the depth value, which is later used as independent variable of the bilateral filter of the AO computation. That means, that for each ray we save the maximum iteration of the linear sample collection, before it is terminated, and normalize this value. The results of the first step are the Monte Carlo AO term, the diffuse term combined with the shadow value, the transparency term, and the depth of the view ray, which are then passed on by framebuffer objects using a texture with four channels.

Step 2 In step two, we apply screen space calculations of the AO calculation. Therefore, we employ the bilateral filter (here we find a kernel size of 13×13 to be sufficient) to the previously computed Monte Carlo AO term.

Step 3 Lastly, in step three, we composite all computed values and generate the final output. Therefore, we assign a color to the fibril as well as the coat. To improve distinctiveness between the semi transparent coat and the sold fibril, we use complementary colors. We apply the AO value of step two to the color of the solid fibril by multiplication. Next, based on the transparency term, which we retrieved in step one, we interpolate the two colors. This interpolation is equal to the interpolation of the illumination values in step one since we use the same transparency value as a basement of the interpolation. Lastly, we just need to multiply our interpolated color values with the diffuse light and shadows, to generate the final output. Further, to generate a more pleasant result, we define a diffuse light color, which is a rather light grey value, and which we then also multiply our result with.

$$C_o = [(1-t) \cdot (C_f \cdot a) + t \cdot C_c] \cdot l \cdot C_l \qquad (9)$$

In Equation 9 a mathematical description of the explained process of combining all retrieved values to generate the final output is described. C_o represents the output color, C_f represents the fibril color, C_c represents the coat color, and C_l represents the color of the diffuse light. Those color values are $\in [0,1]^3$. The fibril color is hence multiplied with the AO a, computed in step two. The interpolation value, retrieved in step one is depicted as t. And l combines diffuse light and shadow value as one illumination term. t and l are scalar values $\in [0,1]$.

7. Technical Evaluation

The non-linear ray marching was directly compared to standard volume rendering in regard of image quality as well as milliseconds per frame and memory consumption. 2D density maps were extracted from a deposited density map at EMDB (accession no. 3132) and published by [SRL*15]. Our hardware setup included a *GeForce RTX 2070 SUPER/PCIe/SSE2* GPU, *AMD Ryzen7 3700X* with 8 cores CPU and 32GB RAM. The viewport had a size of $1920px \times 1080px$.

7.1. Standard volume rendering

Implementing standard volume rendering, using the python based VTK software system [SML06] as well as based on the Inviwo [JSS*] framework, opens the possibility to directly compare the non-linear ray marching with standard volume rendering. To make the approaches comparable, only diffuse illumination is applied. As a transfer function a simple step function is used and camera parameters are adapted between both approaches. The fibril's twist value is adapted to be equal in the standard volume rendering approach and the non-linear ray marching. In Table 1 we compare different resolution settings and resulting memory consumption on the GPU. It is noteworthy that the highest resolution of the underlying 2D density map of our approach does not even use 25% of the memory the standard volume rendering uses for the smallest dense data resolution. As a lower bound we use the comparison of sparse 3D volume data, which only saves occupied voxel data. Therefore, we use the 3D density map of EMD-3132 with a minimum density threshold of 0.4, which corresponds to a voxel occupancy of 17%. It needs to be considered, that sparse memory usually requires an additional data structure to access the appropriate voxels during rendering. Further, memory consumption of volume rendering with sparse data is worse than standard volume rendering. Still, our approach significantly outperforms the lower bound of standard volume rendering with sparse volume data.

Further, we investigated different dense 3D resolutions, which can display the 3D visualization in Figure 6 right. This model has a 1 : 32 width to length ratio. We applied different resolutions and adapted spacing in Standard Volume Rendering to retrieve the depicted models. To compensate increased spacing linear interpolation was applied. But still, for low resolutions in z-dimension and corresponding large spacing in this dimension, artefacts become visible (see Figure 6). Similarly, by decreasing x,y-resolution artefacts appear in Standard Volume Rendering also for high z-resolutions. It seems that in Standard Volume Rendering low resolution in x,y-dimension seems to require high resolution in z-dimension and vice versa. On the other hand, those artefacts are not visible for any resolution of the 2D density map, using the non-linear ray marching (see Figure 6). In fact, visualizations based on low resolution data can hardly be distinguished from visualizations based on high resolution data. The sufficient resolution of the 2D density map exclusively depends on the Nyquist frequency of the underlying signal. Low resolutions might lose information, which can be observed in Figure 6. Still, our approach can visualize those extremely low resolutions without the generation of artefacts. This can further be attributed to the binary search, added to the sample collection (see Section 3.2). Also, using just one 2D density map, the resolution in the third dimension is always adaptable and has no lower bound, hence artefacts, due to low resolution in the third dimension are suppressed in general. And lastly, our approach only requires linear interpolation between texture slices, while standard volume rendering depends on a trilinear interpolation.

Then, we compare the performance of standard volume rendering and the non-linear ray marching. Therefore, we compare milliseconds per frame of standard volume rendering with milliseconds per frame of the non-linear ray marching. We compare against our standard volume renderer based on the VTK software system [SML06], as well as a simple volume renderer based on the Inviwo framework [JSS*]. Again, we used the depicted model in Figure 6, but we altered the volume resolution. As Figure 7 shows, both standard volume rendering approaches outperform our approach for rather small volumes (for memory consumption see Table 1). But with increasing resolution of the volumes, our approach performs significantly better than the implemented volume renderer based on VTK. Further, the volume renderer, based on the Inviwo framework is not able to render volumes with more than 4096 slices, so a comparison to large volume data between our approach and the volume renderer based on the Inviwo framework can not be provided. For small volumes, standard volume rendering outperforms our approach, since the non-linear ray marching introduces additional computations for each sample point along a ray. For larger volumes, which are rather likely in the display of amyloid-beta fibrils, we suspect the better performance of our approach to be attributed to faster texture access. Since our approach only requires so little memory, all the data can be loaded into the cache, hence fast memory access is given at all times. Large volumes of standard volume rendering, on the other hand, can not fully be loaded into the cache, introducing small delays during data access.

7.2. Ray Marching

Further, we investigated the non-linear ray marching, specially focusing on the introduced binary search. As usual, the determination of the ray marching's step size is crucial for image quality. Small step sizes will exceed computational capabilities, while large step sizes might overstep important details and hence lead to artefacts. Based on our proposed binary search to determine the fibril's surface, we are able to keep the step size of the linear sample collection rather high. Additional iterations of the binary search help to improve image quality drastically (see Figure 8). Since we are also adapting the linear step size based on the visible level of detail (see Section 3.2), we only need to apply few iterations of the binary search, to saturate the rendering quality (see Figure 8). In Figure 10 we depict the impact of an additional binary search with 30 iterations for different step sizes. It becomes clear, that rendering quality is improved with the additional binary search, but still, a sufficient step size needs to be chosen, so that surface artefacts can be completely suppressed.

Further, we investigated the impact on performance of the additional binary search. Therefore, we recorded milliseconds per frame for different step sizes, as well as different iterations of the binary search in Figure 9.

Smaller step sizes seem to increase computation time exponentially, while the addition of a binary search only increases the computation time linearly.

8. User Evaluation

To explore the contribution of our newly developed 3D visualization for amyloid-beta fibrils, we further conducted a user evaluation. This evaluation included an expert interview with a PostDoc researcher from the Institute of Protein Biochemistry at Ulm University, as well as a user study, which specially focused on the interpretability of the uncertainty visualization.

8.1. Expert Interview

The interviewed PostDoc researcher deals with specialized research on the topic of amyloid-beta fibrils. He already published valuable contributions to the research in this field. In his research, he regularly makes use of visualization tools based on cryo-EM data. During the interview, we presented him with our 3D visualization live on a screen. Questions were then asked on the phone. In the following, all marked quotes are originated from *Personal interview. 21 August 2020.*

To gain insights about the importance of 3D visualization of the reconstruction, we asked him to summarize, what those visualizations are used for. He explained that a comparison of raw data and the model can be drawn.

> "Visualizations help to explain investigated features of the structure, especially depicting them in publications. [...] Further, we can compare our raw data with the drawn conclusions and results, since the model visualizes this data."

After asking him, if an integration of the provided visualization into a reconstruction tool like Relion would be helpful, he reinforced the suggestion. We questioned him, what current visualization tool he is using in his research. He explained, that he uses USFC Chimera [PGH*04].
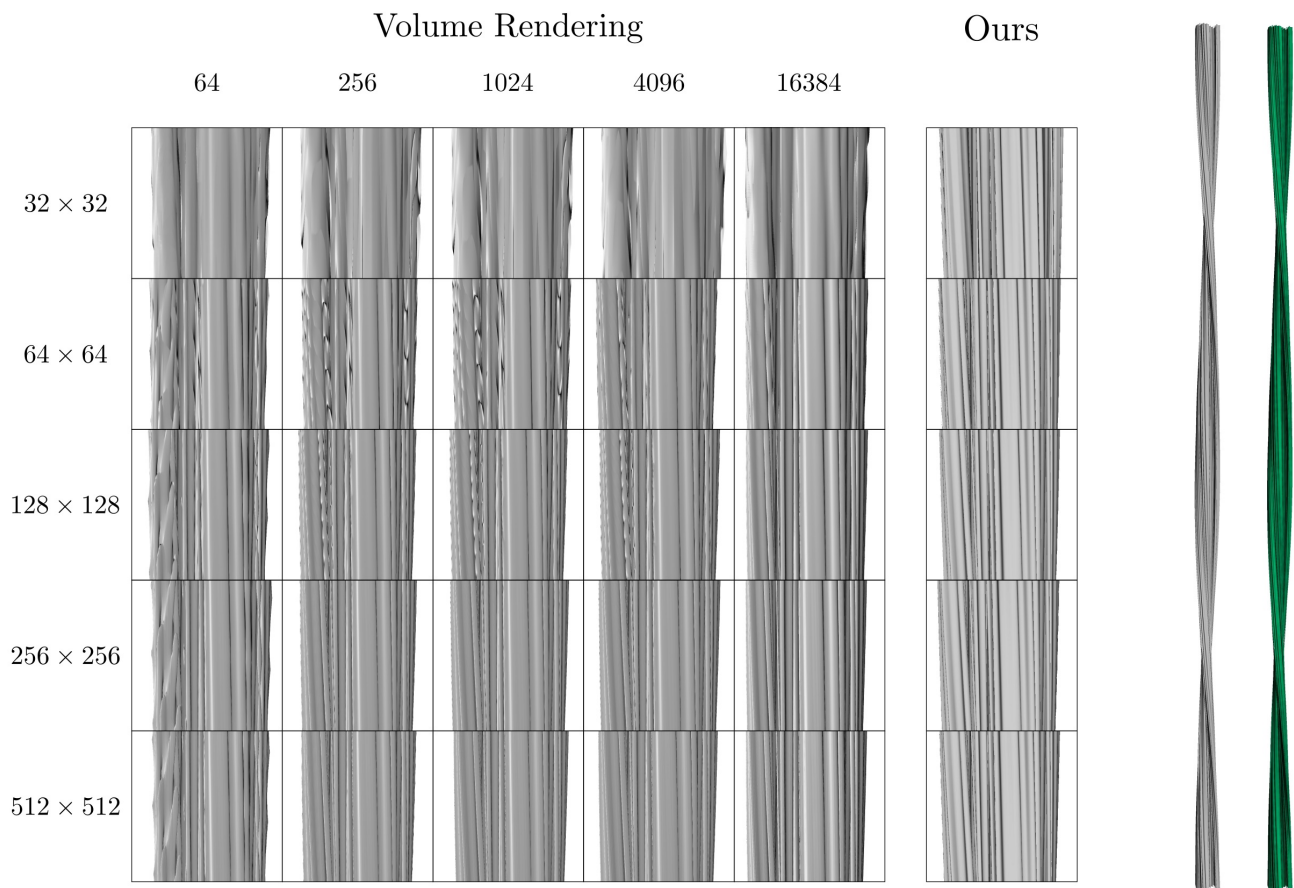
Figure 6: *3D visualizations of a fibril using data from EMD-3132:* **Right** *Two 3D visualizations rendered with our approach. The left model uses Phong illumination only, while all introduced illumination techniques are applied to the right model. The width, length ratio of the shown model accounts* 1 : 32. **Left** *Comparison of image quality of 3D models generated by our approach and Standard Volume Rendering (based on the python VTK [SML06] volume renderer) for different resolutions of the underlying density map. While our approach is hardly distinguishable for any resolution, Standard Volume Rendering generates artefacts for lower resolution data. And still, it has to be noted, that even the lowest resolution in z-dimension of Volume Rendering is 64 times higher than the corresponding resolution of our approach.*

"[...] On its downside, data sizes become large quite fast, if one wants to display long sections of the fibril. Then we are quickly working with data sizes of 1*GB*, which can be problematic. Hence, we often clip this data, to decrease the file size. If we could visualize a detailed version of a large fibril section with fewer data and without going through several steps and using several different programs, that would be beneficial."

We further asked him about his impression of the uncertainty visualization. He replied, that it is a useful feature, which he has not seen in other visualization tools yet. If he wants to depict two different density thresholds of a model, he usually needs to generate two visualizations. Having the uncertainty included directly in one visualization is beneficial, he said. He even suggested going further with this approach: Using multiple thresholds to visualize different densities, that will open the opportunity to compare multiple layers of densities, he explains.

Since the use of our visualization depends on the knowledge of the fibril's twist value, we asked him, if it is a justifiable assumption, that this twist value is known.

"First, one can roughly calculate the twist value based on the crossover of the underlying data. [...] Second, by using Relion for the 3D reconstruction of helical structures, a refined twist value is then calculated based on how well it fits the raw data during reconstruction."

Next, we wanted to know, if there is a benefit of the interactive changeability of the twist. He responded, that this is a feature, he has not seen before, even though it will be of great use.

"The interactive adaption of the twist value is a valuable feature. Based on this feature, one will be able to compare multiple structures."

Lastly, we asked him, if there are possible improvements, he suggests. He stated:
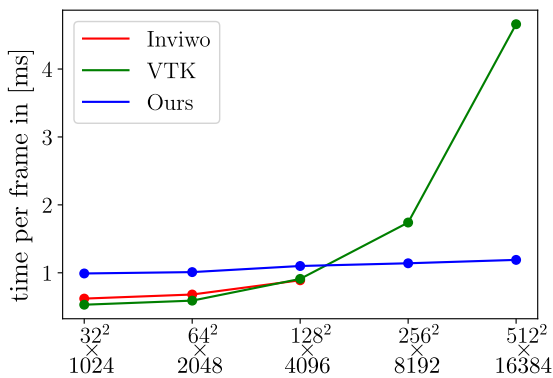
Figure 7: *Comparison of milliseconds per frame of standard volume rendering, based on the python VTK software packages or the Inviwo framework, and our approach for different volume resolutions.*
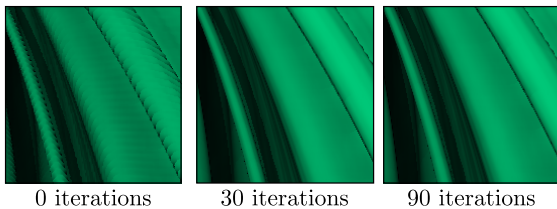

Figure 8: *Impact of binary search iterations in regard of artefact removal: Already a few iterations help to increase image quality greatly.*

"This is a nice visualization tool, which implements beneficial features. It is a suitable tool for resolutions, which are larger than 5Å. Nowadays, resolutions have become better and better. The highest resolution, we were able to achieve was 2.6Å. Hence, to be able to also visualize those high resolutions in detail, it would be necessary to load maybe five 2D density map layers to resolve details of the fibril along the z-axis, which are then stacked to create the visualization of a full fibril.[...]"

He also suggested to then add separate definitions of twist values for each subunit, defined by two consecutive density maps.

Based on this informative interview we can conclude, that our 3D visualization provides first improvements compared to other visualization tools. Especially, the visualization of uncertainty, based on different density thresholds, the interactive twist adaption as well as comparably low memory consumption are major advantages of our approach. The suggestions for improvement are justified proposals. We suspect our algorithm to be easily extendable to those suggestions, by using multiple density maps and linearly interpolating between them. Also, different twist values defined in different subunits are just a matter of definition within the algorithm. A detailed evaluation of those extensions, we leave for future work.
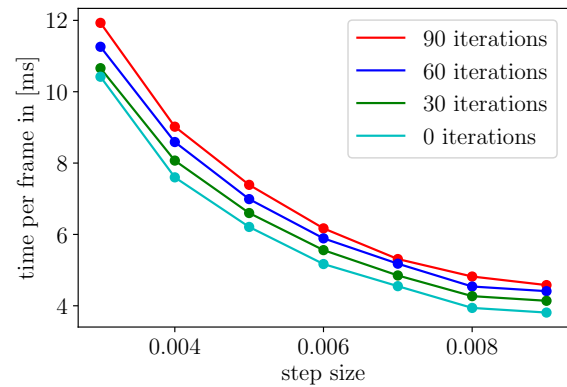

Figure 9: *Impact of binary search iterations in regard of milliseconds per frame.*
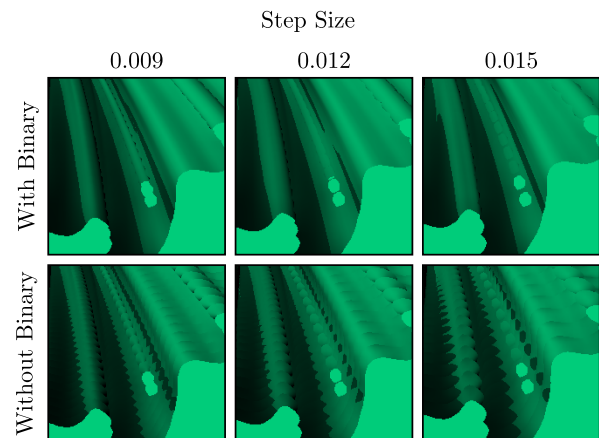

Figure 10: *Impact of additional binary search for different step sizes. Binary search iterations were fixed at 30 to generate the depicted image patches.*

8.2. User Study

To evaluate the interpretability of the semi transparent coat, used for the interactive display of data uncertainty, an online user study was conducted. It was the goal of the study to show the interpretability of the semi transparent coat, so that different inner and outer uncertainty thresholds can be applied by the user to visualize underlying data uncertainty. The main idea was contributed to the question if the observer can distinguish between different levels of uncertainty, hence if the observer can distinguish between relative differences of the underlying densities. This would be the case if the observer can differentiate between different coat depths.

During the study, a total of 34 participants were recruited, without required previous knowledge or specified selection. The survey covered 23 questions in total. For each question two images were shown in a side-by-side manner (see Figure 11). Those images, which were shown in a side-by-side manner, were equal in regard of all parameters (helix structure, view point, light position, etc.)
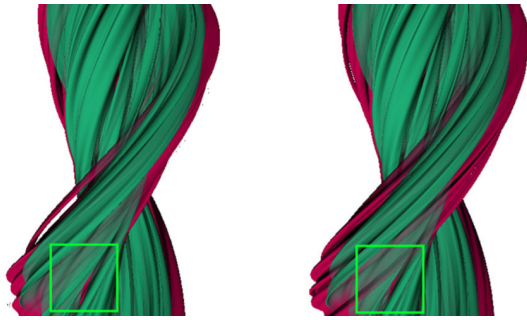
Figure 11: *Side-by-side presentation of two 3D visualization. This image, as well as 22 similar comparisons were shown in the online User Study.*

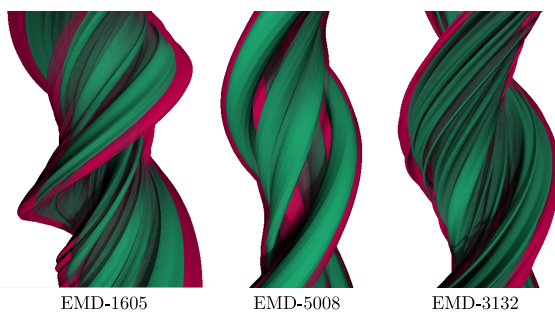EMD-1605   EMD-5008   EMD-3132

Figure 12: *Depiction of three snippets of the used models for the online user study, based on density maps deposited at EMDB. Twist values were altered independent of the structure. Hence, twist values are much higher, than they usually are.*

except for the outer uncertainty threshold. Based on the outer uncertainty threshold the depth of the semi transparent coat was varied. To generate the data three different 2D density maps were used from EMDB (EMD-1650 [SSR*09], EMD-5008 [SFG08], EMD-3132 [SRL*15]). We adapted the twist values of the fibril independent of the deposited structure at EMDB. In Figure 12 three different snippets of the three models are depicted. To generate the data, we varied view point, twist value and inner-, as well as, outer uncertainty threshold (described as t_1 and t_2 in Section 3.2) between the 23 tasks.

The participants were asked to choose the image, showing the fibril with a deeper/thicker semi transparent coat, in a marked area (see Figure 11). All comparisons were shown in random order for each participant. Then, for each participant, the accuracy over all responses was calculated. The accuracies of three participants were significantly below the minimum result of all other participants, suggesting a misunderstanding of the task. Hence, those participants were excluded from all following evaluations. Evaluating the results of all remaining 31 participants were promising (see Figure 13). Approximately 51.61% of all evaluated participants were able to achieve 100% accuracy on all 23 tasks, while only 19.35% performed worse than 90% accuracy. The minimum accuracy reached was 78.26% over all tasks.

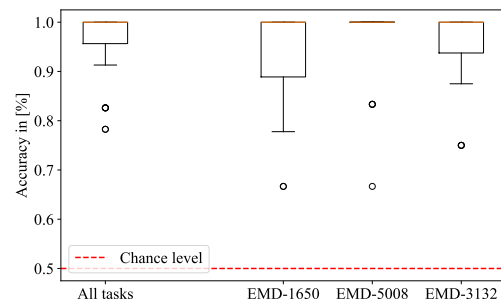**Task wise evaluation** Since three different density maps were

Figure 13: *Accuracy results of 31 participants. The accuracy is calculated for each participant over all 23 tasks and separately for the three different models shown.*

used to create 3D model visualizations, those three groups were also evaluated independently. This was done to create further inside if the shape of the visualized object influences interpretability. Investigated results are shown in Figure 13. The median of 100% is reached for all 3D model visualizations, suggesting that the semi transparent coat can be interpreted well. All in all, for each task, all the participants were able to perform significantly better than the chance level.

In total, the visualization of the semi transparent coat shows a clear trend in the possibility of understanding and interpreting inner and outer uncertainty thresholds, which are directly connected to data uncertainty. The visualization of the coat can therefore be used to communicate different levels of data uncertainty.

9. Conclusion

We have presented an algorithm to visualize 3D amyloid beta fibrils in real-time, which takes as input a single 2D density map. Our algorithm uses a small fraction of the memory used by volume rendering algorithms obtaining an even better time complexity for large volumes and also higher image quality for low resolutions density maps. Our visualization approach makes the visualization of large fibril filaments possible. Further, we provide an algorithm to visualize the underlying uncertainty introduced by noise during data acquisition or errors during 3D reconstruction. Researchers are hence able to compare different levels of density directly at the visualization of the 3D reconstruction. We evaluated this approach by a user study which could show that our approach was able to effectively communicate the uncertainty. An expert interview could underline main benefits of our implementation, like the adaptable twist value, the uncertainty visualization and the required data sizes. It made also clear, that our presented approach is easily extendable for even higher resolutions than 4.8Å. An according implementation and evaluation we will leave for future work.

Moreover, we would like to investigate new visual paradigms to communicate the uncertainty of the data, such as multiple views or glyphs, in the future. And lastly, we would like to explore the challenges of using our algorithm to render scenes composed of multiple fibrils.

Acknowledgements

References

[BHJ*14] Bonneau, Georges-Pierre, Hege, Hans-Christian, Johnson, Chris R, et al. "Overview and state-of-the-art of uncertainty visualization". *Scientific Visualization*. 2014 3.

[CC17] Cressey, Daniel and Callaway, Ewen. "Cryo-electron microscopy wins chemistry Nobel". *Nature News* 550.7675 (2017) 1.

[DCH88] Drebin, Robert A, Carpenter, Loren, and Hanrahan, Pat. "Volume rendering". *ACM Siggraph Computer Graphics* (1988) 2.

[Dei07] Deitrick, Stephanie A. "Uncertainty visualization and decision making: Does visualizing uncertain information change decisions". *XXIII International Cartographic Conference*. 2007 3.

[DLD*15] Dai, Shuangfeng, Lu, Ke, Dong, Jiyang, et al. "A novel approach of lung segmentation on chest CT images using graph cuts". *Neurocomputing* 168 (2015) 3.

[DRN*17] Diaz, Jose, Ropinski, Timo, Navazo, Isabel, et al. "An experimental study on the effects of shading in 3D perception of volumetric models". *The visual computer* 33.1 (2017) 4.

[EHK*04] Engel, Klaus, Hadwiger, Markus, Kniss, Joe M., et al. "Real-Time Volume Graphics". *ACM SIGGRAPH Course*. 2004 2, 3.

[Fra17] Frank, Joachim. "Advances in the field of single-particle cryo-electron microscopy over the last decade". *Nature protocols* (2017) 2, 3.

[HA91] Hardy, John and Allsop, David. "Amyloid deposition as the central event in the aetiology of Alzheimer's disease". *Trends in Pharmacological Sciences* 12 (1991) 1.

[JSS*] Jönsson, Daniel, Steneteg, Peter, Sundén, Erik, et al. "Inviwo - A Visualization System with Usage Abstraction Levels". *IEEE Transactions on Visualization and Computer Graphics* () 6, 7.

[LBG*15] Labschütz, Matthias, Bruckner, Stefan, Gröller, M Eduard, et al. "JiTTree: a just-in-time compiled sparse GPU volume data structure". *IEEE transactions on visualization and computer graphics* 22.1 (2015) 3.

[LR11] Lindemann, Florian and Ropinski, Timo. "About the influence of illumination models on image comprehension in direct volume rendering". *IEEE Transactions on Visualization and Computer Graphics* 17.12 (2011) 4.

[MHK*19] Martschinke, Jana, Hartnagel, Stefan, Keinert, Benjamin, et al. "Adaptive Temporal Sampling for Volumetric Path Tracing of Medical Data". *Computer Graphics Forum*. Vol. 38. 4. 2019 3.

[MOA18] Meiniel, William, Olivo-Marin, Jean-Christophe, and Angelini, Elsa D. "Denoising of microscopy images: a review of the state-of-the-art, and a new sparsity-based method". *IEEE Transactions on Image Processing* 27.8 (2018) 2.

[NS15] Nogales, Eva and Scheres, Sjors H.W. "Cryo-EM: A Unique Tool for the Visualization of Macromolecular Complexity". *Molecular Cell* 58.4 (2015) 2.

[Org19] Organization, World Health. *Dementia fact sheet*. https://www.who.int/news-room/fact-sheets/detail/dementia. Online; accessed 06 July 2020. 2019 1.

[Pan*01] Pang, Alex et al. "Visualizing uncertainty in geo-spatial data". *Proceedings of the workshop on the intersections between geospatial information and information technology*. Vol. 10. 1.20. 2001 3.

[PB07] Preim, Bernhard and Bartz, Dirk. *Visualization in medicine: theory, algorithms, and applications*. 2007 3.

[Pfi05] Pfister, Hanspeter. "Hardware-Accelerated". *Visualization Handbook* (2005) 2, 3.

[PGH*04] Pettersen, Eric F, Goddard, Thomas D, Huang, Conrad C, et al. "UCSF Chimera—a visualization system for exploratory research and analysis". *Journal of computational chemistry* 25.13 (2004) 2, 7.

[Pho75] Phong, Bui Tuong. "Illumination for computer generated pictures". *Communications of the ACM* 18.6 (1975) 5.

[PWL*97] Pang, Alex T, Wittenbrink, Craig M, Lodha, Suresh K, et al. "Approaches to uncertainty visualization". *The Visual Computer* 13.8 (1997) 3.

[RBA09] Reinbothe, Christoph K, Boubekeur, Tamy, and Alexa, Marc. "Hybrid Ambient Occlusion." *Eurographics (Areas Papers)*. 2009 5.

[RG14] Rohou, Alexis and Grigorieff, Nikolaus. "Frealix: Model-based refinement of helical filament structures from electron micrographs". *Journal of Structural Biology* 186.2 (2014) 2.

[RGW*03] Roettger, Stefan, Guthe, Stefan, Weiskopf, Daniel, et al. "Smart hardware-accelerated volume rendering". *VisSym*. Vol. 3. 2003 2, 3.

[SB07] Shen, Rui and Boulanger, Pierre. "Hardware-Accelerated Volume Rendering for Real-Time Medical Data Visualization". 2007 2, 3.

[SC18] Sherman, William R. and Craig, Alan B. "Chapter 6 - Presenting the Virtual World". *Understanding Virtual Reality (Second Edition)*. Boston, 2018 2.

[Sch20] Scheres, Sjors H W. "Amyloid structure determination in RELION-3.1." *Acta crystallographica. Section D, Structural biology* (2020) 2.

[SE16] Sakhaee, Elham and Entezari, Alireza. "A statistical direct volume rendering framework for visualization of uncertain data". *IEEE transactions on visualization and computer graphics* 23.12 (2016) 3.

[SFG08] Sachse, Carsten, Fändrich, Marcus, and Grigorieff, Nikolaus. "Paired beta-sheet structure of an Abeta(1-40) amyloid fibril revealed by electron microscopy". *Proceedings of the National Academy of Sciences of the United States of America* 105.21 (2008) 10.

[SML06] Schroeder, W, Martin, K, and Lorensen, B. *VTK Textbook*. 2006 6–8.

[SMV*14] Simpson, Amber L, Ma, Burton, Vasarhelyi, Edward M, et al. "Computation and visualization of uncertainty in surgical navigation". *The International Journal of Medical Robotics and Computer Assisted Surgery* 10.3 (2014) 3.

[SRL*15] Schmidt, Matthias, Rohou, Alexis, Lasker, Keren, et al. "Peptide dimer structure in an Aβ (1–42) fibril visualized with cryo-EM". *Proceedings of the National Academy of Sciences* (2015) 5, 6, 10.

[SSR*09] Schmidt, Matthias, Sachse, Carsten, Richter, Walter, et al. "Comparison of Alzheimer Aβ (1–40) and Aβ (1–42) amyloid fibrils reveals similar protofilament structures". *Proceedings of the National Academy of Sciences* 106.47 (2009) 10.

[SZD*10] Sanyal, Jibonananda, Zhang, Song, Dyer, Jamie, et al. "Noodles: A tool for visualization of numerical weather model ensemble uncertainty". *IEEE Transactions on Visualization and Computer Graphics* 16.6 (2010) 3.

[ZML19] Zellmann, Stefan, Meurer, Deborah, and Lang, Ulrich. "Hybrid grids for sparse volume rendering". *2019 IEEE Visualization Conference (VIS)*. 2019 3.

[ZSL19] Zellmann, Stefan, Schulze, Jurgen P, and Lang, Ulrich. "Binned kd tree construction for sparse volume data on multi-core and GPU systems". *IEEE Transactions on Visualization and Computer Graphics* (2019) 3.

[ZSX*08] Zhang, Xing, Settembre, Ethan, Xu, Chen, et al. "Near-atomic resolution using electron cryomicroscopy and single-particle reconstruction". *Proceedings of the National Academy of Sciences* 105.6 (2008) 2.